THERMAL TRANSPORT ACROSS INTERFACES WITH MOLECULAR LAYERS

BY

WEI WANG

THESIS

Submitted in partial fulfillment of the requirements
for the degree of Master of Science in Materials Science and Engineering
in the Graduate College of the
University of Illinois at Urbana-Champaign, 2013

Urbana, Illinois

Adviser:

Professor David G. Cahill

Abstract

This thesis presents the experimental study of thermal transport across molecular interfaces. Molecular interfaces are fabricated by assembling Au nanocrystals with controllable surface chemistry onto oxide substrates such as quartz and sapphire. A self-assembled monolayer (SAM) of silane molecules is also grown on sapphire to make the third variety of molecular interfaces. The technique of transient absorption (TA) is used to probe the evolution of Au temperature following abrupt heating by an optical pulse. I modeled the heat transfer from the Au nanocrystals into the molecular coating and then to the substrate and I obtained the values of interfacial thermal conductance of Au/cetyl trimethylammonium bromide/quartz and Au/16-mercapto trimethylammonium bromide/quartz in the temperature range of $40 < T < 300$ K. The room temperature thermal conductance (G) values of these interfaces are both 150 ± 15 MW $m^{-2}K^{-1}$. Low temperature measurements are carried out in an optical cryostat and the temperature dependence of $G(T)$ is found to have the same form as the temperature dependence of the heat capacity of Au. These results suggest the spectrum of vibrational modes that carry heat through the molecular interfaces is similar to the vibrational spectrum of Au; and that anharmonicity does not significantly contribute to the heat transport in this system.

To my parents

Acknowledgments

Throughout my graduate work at the University of Illinois I greatly benefited from the supervision, support, help and guidance provided by my adviser Dr. David Cahill. Besides the enlightening explanations he gave me during the numerous scientific discussions, I am thankful to Dr. Cahill for the extensive support which got me inspired in scientific discovery.

I want to thank my colleagues Dr. Yee Kan Koh, Dr. Wen-Pin Hsieh, Dr. Dong-Wook Oh, Dr. Joseph Feser and Richard Wilson for offering lots of help to me when I began graduate school, with things like the fundamentals of TDTR and phonons, which let me quickly make up the necessary background knowledge in this field. The interactions and scientific discussions with members of this group have been extremely valuable for me (Dr. Xiaojia Wang, Dr. Ji-Yong Park, Tamlin Matthews, Jonglo Park, Trong Tong, Gyunmin Choi, Dongyao Li and people from the Chemistry department: Jingyu Huang and Brandt Pein and of course their faculty advisers). Alongside the academics, I also thank you all for the many moments of joy and delight we spent together.

I am also grateful to the great courses of the MatSE department offered by, for example, Professor Steve Granick, Professor L. B. Freund and Professor John Weaver, which added great value to my graduate school experience.

TABLE OF CONTENTS

CHAPTER 1
INTRODUCTION

1.1 Thermal transport across a molecular interface

An interface connecting two bodies that are held at different temperatures has a finite conductance of heat. The heat is carried by phonons, quanta of lattice vibrations, as the phonons approach the interface, get transmitted/reflected/scattered and move away from the interface. Interfacial thermal conductance G is defined as $J/\Delta T$ [1], where J is the heat flux per unit area across the interface and ΔT is the temperature difference between the two bodies. G has been analyzed under the framework of phonon transmission [1] and in equation (1.1), $C(\omega)$, $t(\omega)$ and $v(\omega)$ are separately the volumetric heat capacity, the transmission probability across the interface and the group velocity of the phonons with frequency ω. G is in principle obtained if the transmission probabilities $t(\omega)$ are known.

$$G = \int C(\omega)t(\omega)v(\omega)d\omega \tag{1.1}$$

Written in the form of $t(\omega)$, the transmission probabilities are assumed to be independent of the temperature on either side of the interface but instead dependent on the material properties of the two bodies. Transmission probabilities across solid-helium and solid-solid interfaces have been calculated by two models: the acoustic mismatch model (AMM) assumes the reflection and transmission of heat-carrying phonons are the same with the reflection and transmission of acoustic waves (the longest wavelength phonons); the diffuse mismatch model (DMM) assumes

the phonons lose their memories on where they came from and their transmission probabilities are decided by the phonon density of states on both sides [1]. Interfacial thermal conductance G calculated from the transmission probabilities predicted by the DMM model agrees well to the experimental data [2,3].

The transmission probabilities of phonons across a *molecular* interface are more difficult to measure and model. Here the interface is referred either to the boundary between a solid and a layer of organic molecules, or to the entire thin layer of molecules (including two boundaries) sandwiched between two solids (figure 1.1), depending on the context. It is postulated that the strong anharmonicity typically found in molecular layers will facilitate three phonon processes within the interface which could either enhance or reduce the interfacial thermal conductance [4,5]. The length scale for the transmitted phonons to come to equilibrium is typically unknown in molecular structures, which raises questions like "what is the temperature" to be used in the definition of interfacial thermal conductance [6]. The limitations with experimental study of thermal transport across an interface become more significant for the interface containing molecular layers: the details of structure and bonding at an interface will matter for its thermal transport property yet interfaces are inherently complex and difficult to characterize; the lack of control and detection sensitivity over individual phonon mode often hinders the sight of what spectrum of vibrational states contributes to thermal conductance across an interface and how the heat moves between the various vibrational states.

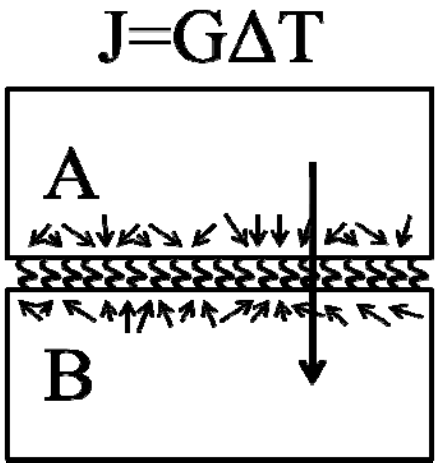

Figure 1.1: Thermal transport across an interface with molecular layers. The small arrows represent the incoming phonons to the interface and the big arrow indicates the direction of heat flow.

With every challenge comes an opportunity. A great deal of interesting science is to be uncovered behind these difficulties, which will be explained in detail below:

Anharmonicity can affect the interfacial thermal conductance *G* in two ways: the three or more phonon processes are not accounted for in the equation of *G* therefore they serve as additional "channels" for heat to be carried across the interface. The additional thermal conductance by three-phonon processes should scale with the temperature *T* at the high temperature limit, since the number of all excited phonons at high temperatures scales with *T*. On the other hand, three phonon processes can reduce the mean-free-paths of phonons hence make the ballistic transport in molecules more diffusive. This can reduce the interfacial thermal conductance. The effect of anharmonicity on interfacial thermal transport is further complicated by the facts that molecular layers also sustain high frequency vibrational modes and they

typically lack a well-defined crystal structure.

These complications can bring about new research areas. One interesting phenomenon mentioned in the literature [7,8] happens in the molecular wires connecting two thermal baths. There the vibrational modes of the molecules are grouped into three categories: low frequency (0-15 THz), intermediate frequency (15-30 THz) and high frequency (>30 THz). The cut-off frequency of the thermal bath lies within the low frequency category (for example, for Au this is 4.5 THz [13]). Anharmonicity at the bonds of contact can convert two phonons from the thermal bath into one intermediate frequency phonon in the molecule, which is otherwise not thermally excited at room temperature. This transport is postulated to be tunneling-like which decreases exponentially with chain length [8]. Measurements of the chain length dependence of the thermal conductance should be able to tell the significance of this heat transfer mechanism.

Mean-free-paths of normal modes in molecular layers are typically unknown yet in many cases they are found to be longer than the length of the molecule itself; therefore the heat flux is ballistic [7]. This nonequilibrium between the heat-carrying modes and the rest modes makes the definition of an interfacial thermal conductance puzzling because although the phonon distribution is probably the same everywhere inside the molecules; it is not thermal. On the other hand, the ballistic transport of heat-carrying modes could be modeled by Boltzmann transport equation (BTE). Since the effects of ballistic carriers on heat transport near a crystal surface are attracting a great deal of attention both in experiment and theory [9,10], it is reasonable to expect that ballistic transport at a molecular interface becomes a field of interest after model systems

have been developed.

One of the limitations with experimental study of thermal transport across an interface is the lack of control and detection sensitivity over individual phonon mode. The most commonly adjusted physical parameter is the temperature. (The temperature jump across the interface is typically small and the saying “temperature of the interface” or “temperature dependence” refers to the temperature of one of the thermal baths or their average temperature) A temperature dependent study can systematically vary the distributions and populations of the incoming phonons to the interface. However, because the Debye density of states of the thermal bath is continuous and the Planck distribution of the heat carriers is broadband, adjusting the temperature always ends up with sending a broadband of phonons to the interface. Similarly, on the detection side, interfacial thermal conductance is an integral quantity which sums up contributions from all incoming phonons. Experimental methods that can differentiate the contributions to thermal conductance by phonons of different frequency groups are uncommon. Molecular layers may offer a unique solution because in many molecules both the heat-carrying and non-heat-carrying vibrational modes can be either Raman or Infra-red (IR) active. The occupation of the heat-carrying modes can be relatively easily obtained from the corresponding anti-Stokes intensity of the Raman spectrum.

1.2 Existing experimental works

Losego et al. [11] fabricated a Au-SAM-quartz interface by firstly growing a silane monolayer (functionalities vary from –SH, -CH_3, -NH_2, -Br etc.) on quartz and then

transfer-printing a Au film onto the SAM-coated quartz substrate. SAM with thiol functionality will bond to the Au film especially after annealing at 115 ^{o}C and SAM with methyl functionality only has van der Waals interaction with the Au film. The strength of the bonding (i.e. interfacial bond stiffness) has been characterized with picosecond acoustics and laser spallation experiments. The interfacial thermal conductance is measured by time domain thermoreflectance [12] and a quantitative link between the interfacial bond stiffness and the thermal conductance is built up.

Perhaps more uniquely, their method of creating a molecular interface is facile and universal, allowing the systematic tuning of the interfacial bond strength, molecular length, molecular type (silane SAM, polymers, etc.) and molecular density.

Good contact between the molecular layer and the solid is difficult to realize experimentally. A key ingredient of their work is the usage of a layer of PVA that is cast onto the Au surface before the transfer-printing, to impart mechanical stability of the Au film. The molecules grown on quartz substrate have a thickness of 1-2 nm so in order to bring the Au film into good contact with the molecules, the flatness of the film must be ensured. Since the Au film grown from thermal oxide on Si is flat with a roughness below 1 nm, a good contact for the molecular interface can be guaranteed as long as the Au film is mechanically stabilized during transfer printing.

Ong et al. [13] synthesized spherical nanocrystals (including CdSe, PbS, PbSe, PbTe, Fe_3O_4 and Au) that were capped with organic or inorganic ligands (including oleic acid, nonanoic acid and $(N_2H_5)_2In_2Se_4$ etc.) and assembled these nanocrystals into crack-free, close-packed

hexagonal nanocrystal array (NCA) in the form of thin films spun-cast on silicon substrates. The core diameters of the nanocrystals and the thicknesses of the films were all controllable. A transducer Au film was evaporated on these films by e-beam evaporation and the thermal conductivities of the films are measured by the frequency domain thermal reflectance (FDTR) technique. The thermal conductivity of the nanocrystal array can only be modeled by the effective medium theory that incorporates a thermal conductance h at the nanocrystal-ligand interface. The thermal conductance is shown to be dependent on the nanoparticle composition. Temperature dependence of the thermal conductivity of the NCA films always shows a plateau above the Debye temperature of the nanocrystal, indicating the dominance of elastic scattering events at the nanocrystal-ligand interface.

The broad selection of the composition of nanocrystals and ligands as well as the control of core diameter and superlattice spacing are remarkable features of this work, which also demonstrate that nanocrystal array is an ideal platform for the systematic experimental study of interfacial thermal transport. They found the interfacial thermal conductance was limited by the upper bound of the nanocrystals' vibrational spectra and the thermal conductivity of the composite material can be increased by using a core material of high Debye temperature.

Making nanocomposites with high density of interfaces is an ingenious strategy to create molecular interface and study its thermal transport property. The molecular layer at interfaces becomes the matrix material of the nanocomposites. A key ingredient to the correct modeling of the NCA thermal conductivity is the bulk thermal conductivity of the matrix material. The

authors deftly employed the thermal conductivity of the wax-like lead oleate as the thermal conductivity of the matrix material because in both materials the oleic ligand is bounded. On the other hand, this approximation does not take into account the full complexity of the thermal conductivity of the matrix.

1.3 References

[1] E. Swartz and R. Pohl, Rev. of Mod. Phys. **61**, 605 (1989).

[2] R. M. Costescu, M. A. Wall, and D. G. Cahill, Phys. Rev. B **67**, 054302 (2003).

[3] W. P. Hsieh, B. Chen, J. Li, P. Keblinski, and D. G. Cahill, Phys. Rev. B **80**, 180302 (2009).

[4] H. K. Lyeo and D. G. Cahill, Phys. Rev. B **73**, 144301 (2006).

[5] T. Luo and J. R. Lloyd, Int. J. Heat Mass Transfer **53**, 1 (2010).

[6] D. G. Cahill, W. K. Ford, K. E. Goodson, G. D. Mahan, A. Majumdar, H. J. Maris, R. Merlin, and S. R. Phillpot, J. Appl. Phys. **93**, 793 (2003).

[7] D. Segal, A. Nitzan, and P. Hänggi, J. Chem. Phys. **119**, 6840 (2003).

[8] T. Luo and J. R. Lloyd, Int. J. Heat Mass Transfer **53**, 1 (2010).

[9] M. E. Siemens, Q. Li, R. Yang, K. A. Nelson, E. H. Anderson, M. M. Murnane, and H. C. Kapteyn, Nature materials **9**, 26 (2009).

[10] A. J. Minnich, J. Johnson, A. Schmidt, K. Esfarjani, M. Dresselhaus, K. A. Nelson, and G. Chen, Phys. Rev. Lett. **107**, 095901 (2011).

[11] M. D. Losego, M. E. Grady, N. R. Sottos, D. G. Cahill, and P. V. Braun, Nature Materials **11**, 502 (2012).

[12] D. G. Cahill, Rev. Sci. Instrum. **75**, 5119 (2004).

[13] W. L. Ong, S. M. Rupich, D. V. Talapin, A. J. H. McGaughey, and J. A. Malen, Nature Materials **12**, 410, (2013)

CHAPTER 2
EXPERIMENTAL METHODS

2.1 Transient absorption

2.1.1 Apparatus

The majority of this thesis work is to study the thermal transport around Au nanorods. The experiment has always been carried out on a transient absorption apparatus and the sample has always been Au nanorods whether they are supported on substrates such as quartz and self-assembled monolayer-covered sapphire, or suspended in liquids such as water and methanol.

Transient absorption is the most fundamental variety of femtosecond pump probe experiments and it has been used by a number of groups to study the ultrafast dynamics of electrons and lattice of metal nanoparticles [1,2] as well as the thermal transport from the nanoparticles to their surroundings [3-6]. In a typical pump probe experiment, a pump pulse is sent in to excite the electrons in the metal nanoparticles via plasmonic absorption. The lattice of the nanoparticle is soon heated via quick electron-lattice scattering and the heat starts to dissipate into the surroundings. Next, a time-delayed probe pulse is sent in to measure the evolution of the lattice temperature through the temperature dependence of the optical absorption.

The pump probe signal of Au nanorods arises from the broadening of its absorption peak, known as longitudinal surface plasmon resonance (LSPR) following pulsed laser heating of the Au nanorod [7]. The signal is strongest, i.e. the change in absorption is biggest, when the probe

is at the wavelength of peak absorption. Temperature change of the environment can also contribute to the signal by inducing a red or blue shift in the LSPR [5], which is least significant at the peak wavelength. Therefore it is desirable to tune the laser to the peak wavelength of the sample to both maximize the signal from Au nanorods and minimize signal from the environment. The optical absorption of Au nanorod at LSPR is well modeled by the Gans theory [8] and it is a strong function of the aspect ratio as well as the dielectric constants of Au and the surrounding medium [9].

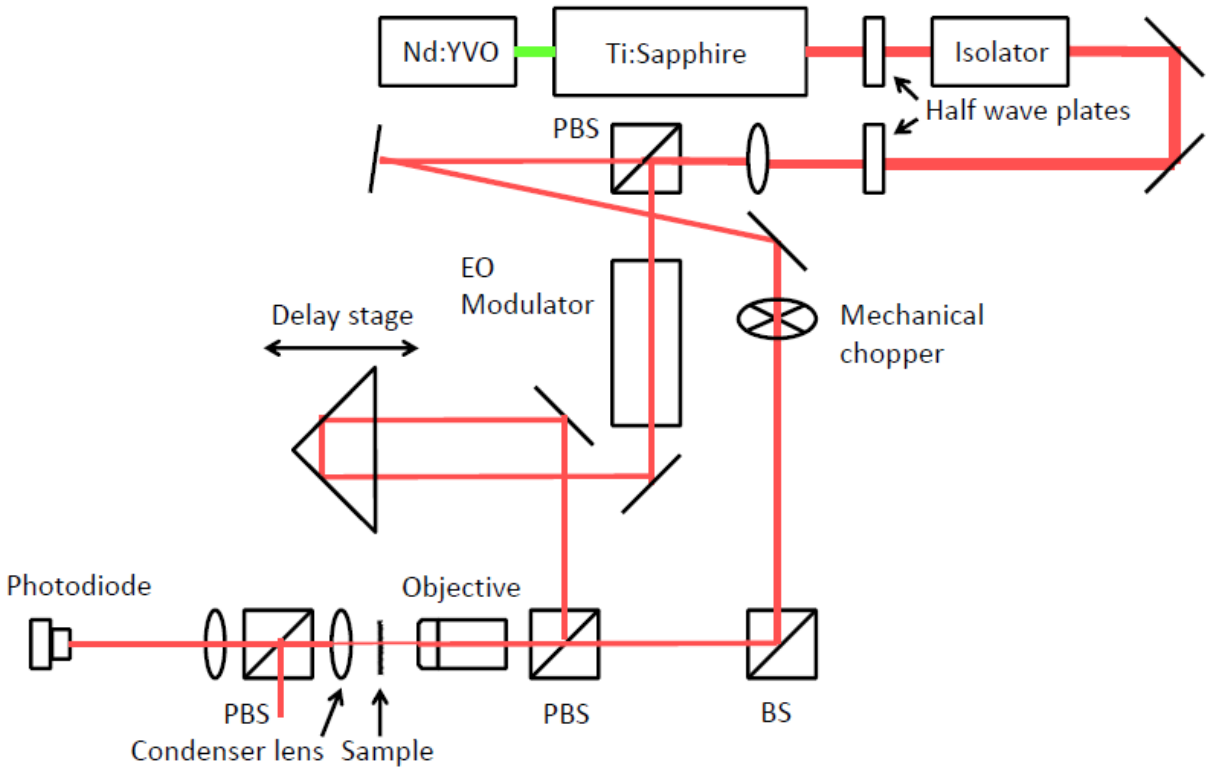

Figure 2.1: Schematics of the optical layouts for transient absorption.

The optics layout of the apparatus is given by figure 2.1. A mode-locked Ti:sapphire oscillator outputs a series of laser pulses at a repetition rate of 80 MHz and the duration of each pulse after multiple dispersions is on the order of one picosecond. The laser beam is split into a

pump beam and a probe beam, the intensities of which can be adjusted using half waveplates and polarizing beam splitters. The pump beam is then modulated by a square wave of 9.8 MHz using an electro-optical modulator (EOM) and then time-delayed by a mechanical delay stage. Note in our implementation the arrival time of the pump pulse is gradually advanced as the delay time increases. The probe beam is chopped by a mechanical chopper at 200 Hz. Unlike our TDTR apparatus [10] no optical filters were used for the purpose of spectral separation of the pump and probe beams. This is because I need to tune the laser wavelength to the peak absorption wavelength of the sample, which can be any arbitrary value between 740 nm and 840 nm depending on our sample preparation. The cross-polarized beams are directed into a 5x objective lens in parallel and focused onto a circular spot with 10.3 μm as the radius of $1/e^2$ intensity. The separation of the two beams is 4 mm. The sample surface is brought to the focal plane of the objective lens with the aid of a f = 400 mm lens and a CCD camera. The transmitted pump and probe beams are re-collimated with a condenser lens. A polarizing beam splitter blocks out the transmitted pump beam and the transmitted probe beam is measured by a photodiode. The photodiode outputs a current to a 50 Ω load inside a pre-amplifier and the resultant voltage is amplified by 5 times. An inductor is placed on the path to the pre-amplifier to form a resonant circuit with the photodiode: the sine wave component of the signal at 9.8 MHz is amplified by 11 times while all higher order harmonics from the square wave modulation are filtered. The filtered and amplified signal is then transmitted to a lock-in amplifier which outputs a square wave of its in-phase display to a computer lock-in system. The square wave is due to the mechanical

chopping of the probe beam at 200 Hz and the data from the computer lock-in is finally collected by a labview program.

The change in optical absorption/transmission of the nanorods per unit temperature rise, i.e. thermotransmittance ($\Delta Tr/\Delta T$), is of interest to the nanophotonics community. The temperature rise ΔT of Au nanorods can be calculated from the following parameters: per pulse energy of the pump beam, the percentage of absorption, the volume of Au within the laser focal spot that absorbs light and the volumetric heat capacity of Au. Note the volume of Au nanorods which absorb laser light is only a small fraction of the volume of Au nanorods within the laser focal spot [6]. Determination of the change in transmission of Au nanorods from the in-phase data collected by the labview program requires the following knowledge: the in-phase data from the labview program is an expansion of the in-phase signal displayed on the lock-in amplifier. When the in-phase data reaches 63.65, the in-phase display of the lock-in amplifier reaches the full scale of the selected sensitivity. The in-phase display of the lock-in amplifier has a form of square wave at 200 Hz. Its peak-to-peak voltage V_{pk} is the rms amplitude, i.e. 1/sqrt(2) of the amplitude of the sine signal coming from the pre-amplifier. The amplitude of the sine signal from the pre-amp is 55 times $2/\pi$ times the peak-to-peak variation of the voltage over the 50 Ω load inside the pre-amplifier, which is related to the change in optical transmission by the same factor that relates the voltage over a 50 Ω load to the transmission of the nanorods. Here is an example: suppose the voltmeter reading over a 50 Ω load within the same circuit is 9.4 mV. The voltage reading should be 18.8 mV when the chopper is open. The transmission of the sample is

determined by UV-vis to be 0.826 at the laser wavelength. The in-phase data from the labview program is a function of delay time t which is represented by $V_{in}(t)$. Then the in-phase display on the lock-in amplifier is $V_{in}(t)/63.65*$sensitivity. The peak-to-peak variation over the 50 Ω load inside the pre-amp is then $V_{in}(t)/63.65*$sensitivity$/(55*2/\pi/\mathrm{sqrt}(2))$. The change in optical transmission is $V_{in}(t)/63.65*$sensitivity$/(55*2/\pi/\mathrm{sqrt}(2))$ /18.8mV*0.826.

More explicitly, the change in the sample's optical transmittance ΔTr(t) (in %) [11] is calculated from the in-phase voltage $V_{in}(t)$ using the following equation:

$$\frac{\Delta Tr(t)}{Tr} = \frac{\Delta V_{in}(t)}{2V_0}\frac{\sqrt{2}}{gQ}\frac{\pi}{2} \qquad (2.1)$$

where t is the delay time, Tr is the optical transmittance of the sample at the laser wavelength, $2V_0$ is the output voltage of the photodiode when the chopper is open, g=5 is the gain of the preamplifier, Q=10 is the quality factor of the resonant circuit and the factor π/2 accounts for the amplitude reduction when a square wave signal is filtered to its first harmonic component.

2.2 Low temperature measurements

I used a helium transfer line to transfer liquid helium into the optical cryostat. Before the transfer of helium, the sample needs to be loaded into the cryostat with the space inside the cryostat pumped down to below $1x10^{-6}$ mbar. To transfer liquid helium, I first lowered down a low-loss transfer tube (model number: LLT700) from the ceiling until one leg of the transfer tube is inserted into a dewar containing liquid-helium. The dewar is then filled with helium gas until the internal pressure goes to 10 psi. The needle valve on the transfer tube is opened by one turn

so that the internal space within the transfer tube can be vented with helium gas. This step is needed (3 minutes should be long enough) because the transfer tube is initially filled with air which will freeze and block the capillaries of the transfer tube when the leg (made of steel) is immersed in liquid helium. If this happens, the transfer tube needs to be pulled out and heated by a drying gun. Once the transfer tube is filled with helium gas, the outlet of the transfer tube is inserted into the center of the optical cryostat and the helium transfer begins. The sample holder is thermally anchored to a cold finger and the temperature of the cold finger is controlled by simultaneous cooling by the liquid helium and heating by an inset heater. The temperature of the cold finger is measured by an inset thermocouple and the power of the heating is feedback-controlled by a ITC temperature controller.

The cryostat I used is the model Microstat^{TM} He from Oxford instrument. The cryostat leg is comprised of a stainless steel tube, a cold finger and a sample holder. The liquid helium vaporizes at the end of the tube which in turn cools down the cold finger. The cryostat leg is mounted inside an outer vacuum chamber (OVC). Air is pumped off from the chamber to prevent convective heat transfer or air condensation to the cryostat leg.

Because the volume of the Au nanorods is exceedingly small compared to a film of equivalent thickness, even a small amount of ice condensed on the surface of the sample will significantly alter the evolution of the nanorod temperature. The vacuum level inside the cryostat is lower than the reading from the gauge since according to the design, air is pumped off through a very narrow opening. The gas adsorbed to the inner surface of the outer vacuum chamber is

mostly water after the chamber is pumped down for a few hours. The outgassed water will deposit line-of-sight onto my sample once the sample is cooled down to low temperatures, while the outer vacuum chamber is maintained at room temperature and continue outgassing. To avoid water condensation on my sample, I used a glass window to protect the sample surface (figure 2.2). Air within the formed space is pumped off from a trench cut onto the sample holder; the glass window both blocks the direct deposition of water and serves as a cold trap if some water molecules diffuse into the space. The same measures were used in a previous work [12].

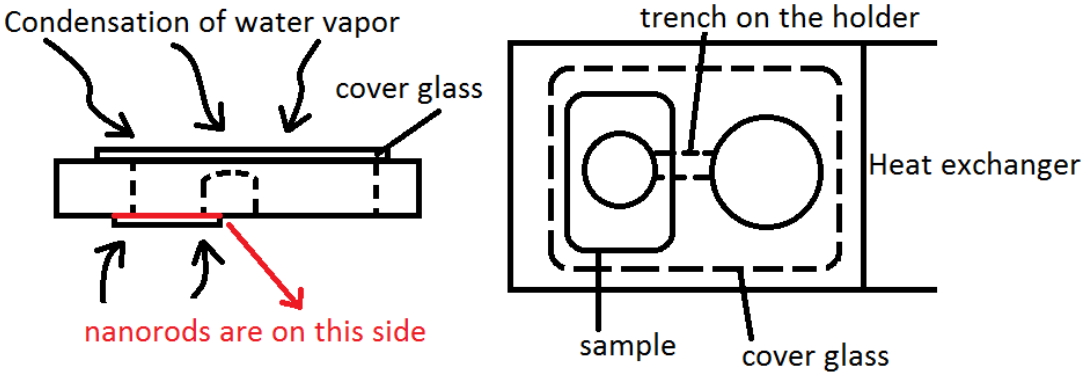

Figure 2.2: Condensation of water vapor on the sample is prevented by a glass window.

2.3 References

[1] C. Voisin, N. Del Fatti, D. Christofilos, and F. Vallée, J. Phys. Chem. B **105**, 2264 (2001).

[2] J. H. Hodak, I. Martini, and G. V. Hartland, J. Phys. Chem. B **102**, 6958 (1998).

[3] Z. Ge, D. G. Cahill, and P. V. Braun, J. Phys. Chem. B **108**, 18870 (2004).

[4] J. Alpert and K. Hamad-Schifferli, Langmuir **26**, 3786 (2010).

[5] J. Huang, J. Park, W. Wang, C. J. Murphy, and D. G. Cahill, ACS nano **7**, 589 (2012).

[6] J. Park, J. Huang, W. Wang, C. J. Murphy, and D. G. Cahill, J. Phys. Chem. C **116**, 26335 (2012).

[7] G. V. Hartland, Phys.Chem.Chem.Phys. **6**, 5263 (2004).

[8] R. Gans, Annalen der Physik **352**, 270 (1915).

[9] S. Eustis and M. A. El-Sayed, J. Appl. Phys. **100**, 044324 (2006).

[10] K. Kang, Y. K. Koh, C. Chiritescu, X. Zheng, and D. G. Cahill, Rev. Sci. Instrum. **79**, 114901 (2008).

[11] D. G. Cahill, Rev. Sci. Instrum. **75**, 5119 (2004).

[12] Wang, W.; Cahill, D. G. *Phys. Rev. Lett.* **2012***, 17,* 175503.

CHAPTER 3
TEMPERATURE DEPENDENCE OF THE THERMAL CONDUCTANCE OF AU/SELF-ASSEMBLED MONOLAYER/QUARTZ INTERFACES

Parts of chapter 3 will be published in "Temperature dependence of the thermal conductance of Au/Self-assembled monolayer/quartz interfaces" by Wei Wang, Jingyu Huang, Catherine J. Murphy, and David G. Cahill, *in preparation*

3.1 Synthesis and characterization

I created the molecular interfaces by assembling positively charged Au nanorods onto negatively charged substrates. The coating molecules on Au nanorods are either cetyltrimethylammonium bromide (CTAB) or 16-mercaptohexadecyltrimethylammonium bromide (MTAB). The negatively charged substrates include quartz, sapphire and self-assembled silane monolayer on sapphire.

3.1.1 Synthesis of CTAB-coated Au nanorods

The Au nanorods were synthesized using a surfactant-directed seeded growth method [1]. The seed solution is obtained by adding 0.6 mL of 0.01 M ice cold $NaBH_4$ solution to a mixture of 250 μL of 0.01 M $HAuCl_4$ and 9.75 mL of 0.1 M CTAB solution. The seed solution was capped and stirred for half an hour and then aged for four hours before use. The growth solution was made by mixing 15 mL of 0.01 M $HAuCl_4$ solution with 285 mL of 0.1 M CTAB solution,

to which 2.7 mL of 0.01 M $AgNO_3$ solution was added. Next, 1.65 mL of 0.1 M ascorbic acid solution was added and the color of the Au(III) solution quickly disappeared. Finally 360 μL of seed solution was added to the above colorless solution and the reaction mixture was aged overnight. All solutions are made from deionized ultrafiltration water generated by Barnstead Nanopure water purification system. Empirically, the average aspect ratio of the Au nanorods is controlled by the amount of silver added and the average diameter of the Au nanorods is controlled by the diameter of the Au seeds.

Au nanorods exhibit unique optical properties due to its longitudinal surface plasmon resonance (LSPR). The concentration and aspect ratio (A.R.) of the Au nanorods in aqueous solution can be determined by their absorbance spectra acquired using a Cary 500 UV-vis-NIR spectrophotometer: A.R.=(λ_{max}-420.3)/95.07 [2] where λ_{max} is the maximum absorption wavelength. The extinction coefficient ε=0.0123*λ_{max}-5.0192 in unit of $nM^{-1}cm^{-1}$ [5] from which the concentration can be calculated. A typical UV-vis absorbance spectrum of Au nanorods in 0.1 M CTAB solution is shown in figure 3.1.

Au nanorods are purified by centrifugation. 50 mL as-grown Au nanorods solution is centrifuged at a speed of 11000 rpm for 20 minutes and the supernatant is removed by a glass pipet that is connected to a vacuumed flask. The nanorod pellet, having a volume of 0.05 mL to 0.1 mL, is then diluted to 50 mL by deionized water and centrifuged again. The free CTAB concentration in the resultant pellet (0.05 mL - 0.1 mL) is 0.1 - 0.2 mM. I diluted the pellet to about 1 nM for usage in the next step and the free CTAB concentration is reduced to a few μM.

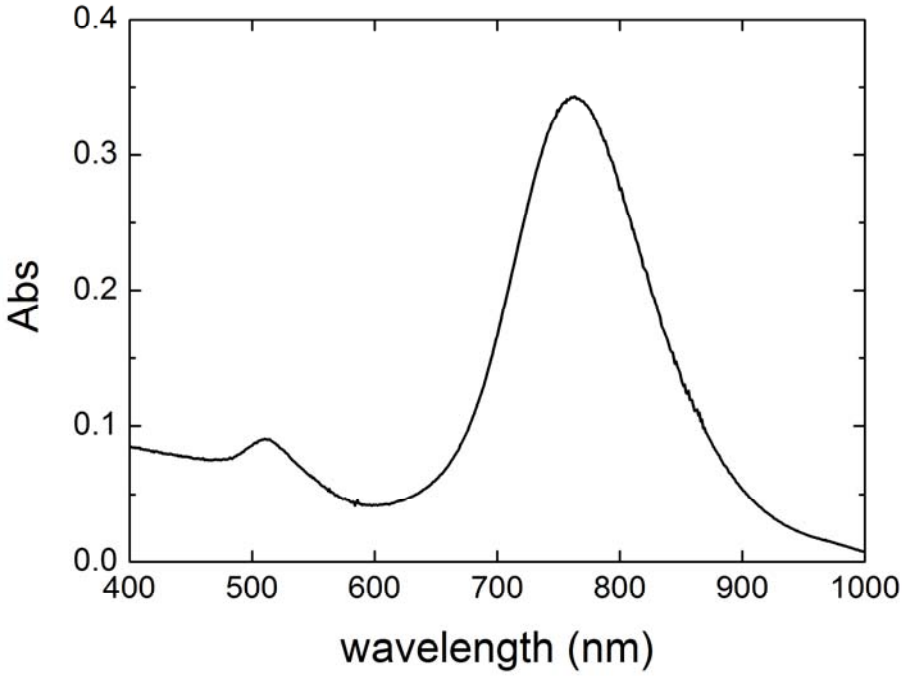

Figure 3.1: UV-vis absorbance spectrum of Au nanorods in 0.1 M CTAB solution

3.1.2 Synthesis of 16-mercaptohexadecyltrimethylammonium bromide (MTAB)

I synthesized the MTAB using a modified version of the reported method [3]. The scheme of the reactions is shown in figure 3.2 and some experimental observations are discussed below.

In the first step, when THF was removed by rotary evaporation after the reaction, I obtained a black, agglomerated, sticky product. The stickiness of the mixture was caused by the wax-like property of the product **1** and unreacted PPh_3 and NBS, existing in the form of the salt $(BrPPh_3)NS$, and the side products ($OPPh_3$ and NHS) are also present. While the reported method directly re-crystallized the mixture from ethanol, I first got rid of the impurities by breaking the solid into smaller granules and extracting **1** out of the mixture using refluxing

hexane. Recrystallization was easier to do with the extracted **1** (50% isolated yield).

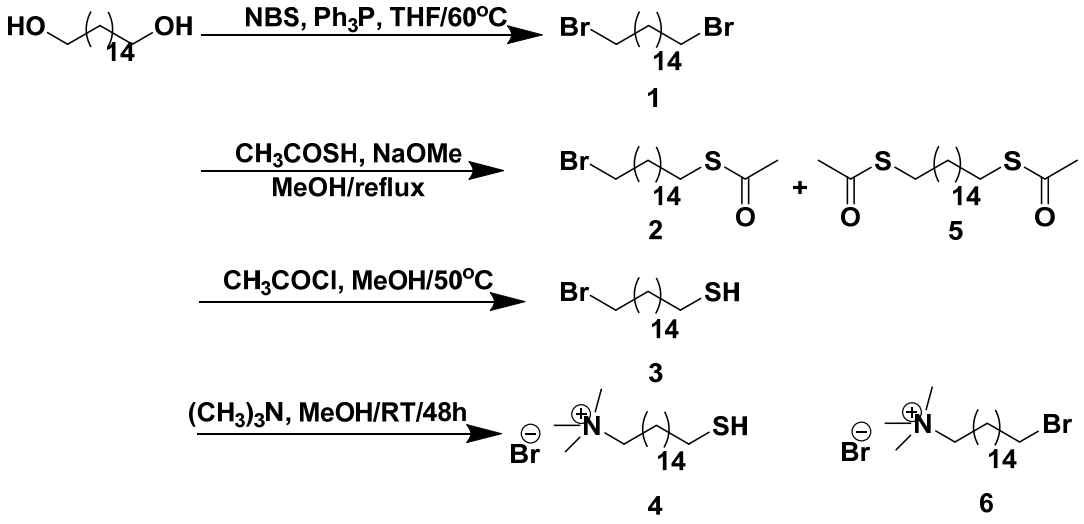

Figure 3.2: Scheme of chemical reactions involved in the synthesis of MTAB.

In the second step, I observed colorless oil after the solvent methanol was removed by rotary evaporation. The oil solidified when it was cooled by ice. I used pure hexane instead of 20% ethyl acetate in hexane as the eluent for column chromatography. The unreacted 1 went out first and desired product **2** went out next.

In the fourth step, the final product was further purified by recrystallization from 20:1 (v:v) ethyl acetate and methanol.

3.1.3 Atomic structure and colloidal stability of CTAB-coated, MTAB-coated nanorods

The surface facets of Au nanorods prepared by the seed-mediated, surfactant-assisted growth technique [1,8] have been determined from the 3D reconstruction of HAADF-STEM images [9]: the cross-section of the rod is bound by alternating {100} and {110} planes and the ends are bound by alternating {101}/{011} and {111} planes. Therefore the entire nanorod can

be approximated as an octagonal cylinder.

Au nanorods grown from the solution are initially coated with a bilayer of CTAB surfactant (about 4 nm in thickness) [10] with bonding between the tertiary ammonium groups and the Au nanorod [5] (figure 3.3). It is believed that a layer of bromide anions are chemisorbed to the surface sites of Au nanorods [5] and the inner leaflet of cetyltrimethylammonium (CTA) cations binds to the bromide anions electrostatically. The hydrophobic tails of the inner and outer CTA leaflets form a hydrophobic layer. The Au nanorods are stabilized by the positive charges of the outer CTA leaflet which induces interparticle repulsion.

The colloidal stability of Au nanorods against centrifugation depends on the concentration of CTAB in the solution. According to my experiences, nanorods purified by centrifugation in a > 1 mM CTAB solution will form a re-dispersible pellet, the interparticle distance of which is about a few hundred nanometers. Nanorods purified by centrifugation in 1 μM CTAB solution will irreversibly aggregate and no solvent can dissolve them again. The centrifugation pushes the nanorods closer, which forms a balance with the interparticle repulsive force. Evidences of nanorod aggregation in solution phase include significant broadening or red shifting of the LSPR absorption as well as fading of the characteristic color of the nanorods. [5]

The CTAB in the nanorod solution will screen the charge attraction between the quartz and the nanorods, which prevents reproducible fabrication of a good CTAB-nanorod sample, but it is impossible to completely remove CTAB since its stabilizing ability depends on its concentration in the solution. Moreover, ethanol can rinse off part of the CTAB coating around Au nanorod and

it is difficult to characterize the amount of the remaining CTAB around Au nanorods.

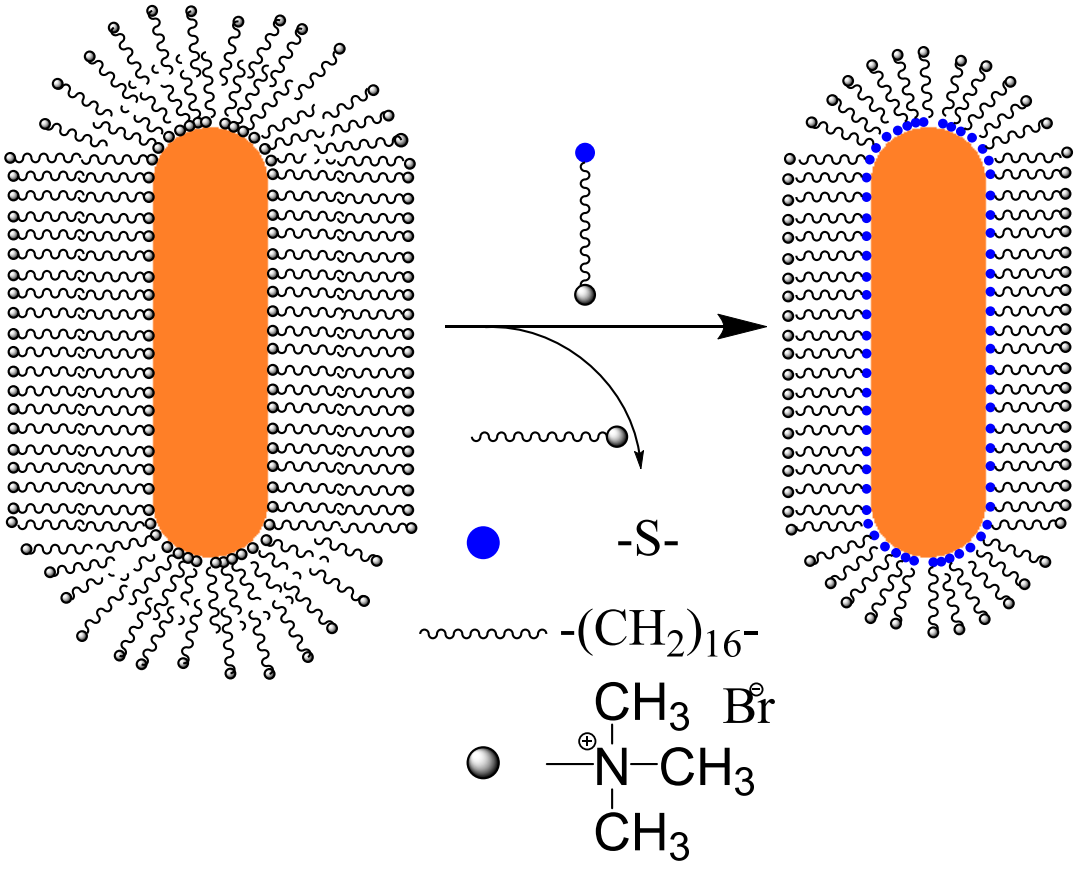

Figure 3.3: Replacement of the CTAB bilayer with MTAB monolayer

Replacement of the CTAB bilayer with a MTAB monolayer greatly improves the above situation. A monolayer of MTAB molecules can completely replace the bilayer CTAB by forming covalent Ag-S or Au-S bonds [3] while the particles maintain a positive charge. The replacement is carried out by mixing high concentrations of CTAB-coated nanorods with MTAB solution [3]: 800 mL as-synthesized CTAB nanorod solution was centrifuged twice, from which 1 mL of ~100 nM nanorod pellet was obtained. The free CTAB concentration in this pellet was 0.2 mM. 24 mg of MTAB was dissolved in 0.6 mL warm water and the solution was added to the

pellet. The mixture was stirred for 12 hours. The purification of MTAB nanorods was done by 4 cycles of centrifugation at 8000 rpm. The purification reduced the free CTAB and MTAB concentrations by a factor of $2x10^9$ if one assumes the free surfactant molecules and the nanorods are fully dispersed when the pellet is diluted by pure water.

The MTAB nanorods exhibit many interesting properties: the MTAB nanorods dissolve and disperse well in methanol (figure 3.4); they can be precipitated out from aqueous solution by acetone and the precipitation can be re-dissolved by methanol and ethanol; they can be purified by centrifugation to as many as 15 cycles (the solution is diluted by 100 times in each cycle) and still exhibit LSPR absorption at its primary wavelength. UV-vis absorption spectra of MTAB nanorods during seven cycles of purification are given in the literature [3], showing that no aggregation and no change in average aspect ratio have happened to the MTAB nanorods.

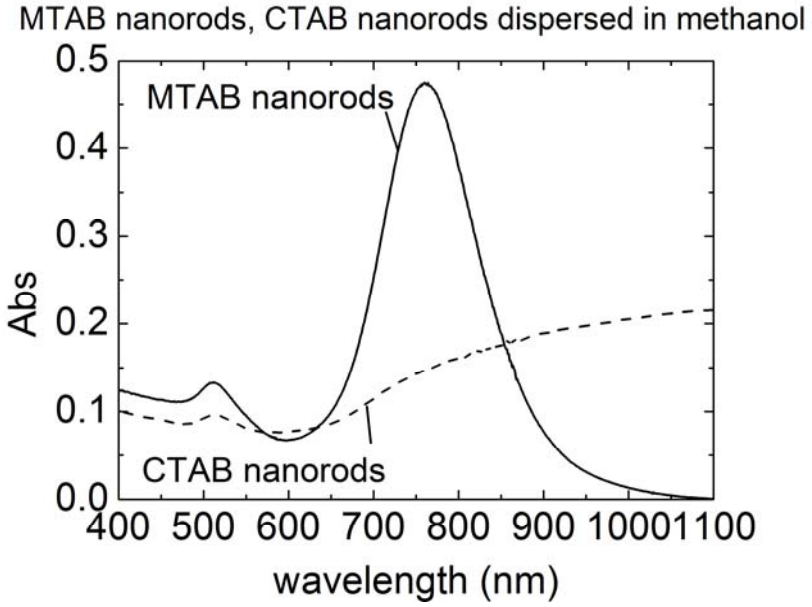

Figure 3.4: UV-vis absorption spectrum of MTAB- and CTAB- nanorods dispersed in methanol.

Vigderman et al. [3] also observed the non-existence of methyl group in the NMR spectrum of any of the liquids during the digestion of the purified MTAB-nanorods, suggesting the CTAB has been completely removed from the Au surface by MTAB.

3.1.4 Preparation of 11-carboxyundecyl trimethoxy silane (CTMS)/sapphire

To prepare SAM-sapphire, I first grew a monolayer of 11-cyanoundecyl trimethoxy silane (YTMS) on sapphire and then converted YTMS to negatively charged functionality (CTMS) by hydrolyzation. The sapphire substrate was cleaned by piranha (3:1 v:v H_2SO_4:H_2O_2) before use. A dry sapphire wafer was immersed in 2.5 mM YTMS toluene solution for 24 hours according to a method reported in the literature [4]. The sample of YTMS functionalized sapphire needed to be sonicated in toluene for 10 minutes to remove dusts and polymer particles. Next, the sample was immersed in a slowly stirred 0.6 mM $NaHCO_3$ solution for 2 days to convert YTMS to CTMS.

I measured the interfacial thermal conductance of CTAB-nanorods/CTMS/sapphire as a function of temperature and found the thermal conductance dropped faster than the heat capacity of Au when the temperature went down to 40 K. This can be interpreted as the molecules (CTAB and CTMS) only allow higher frequency phonons to transmit across the interface. I also characterized the thickness of CTMS by X-ray photoelectron spectroscopy (XPS). However I wasn't able to reproduce the monolayer of CTMS with the same XPS thickness later on, so here I did not report the thermal conductance data for this variety of molecular interface.

3.1.5 Immobilization of CTAB-coated, MTAB-coated nanorods on quartz

Procedures for the assembly of MTAB-coated Au nanorods on quartz were developed and described below: single crystal quartz wafers were first activated by piranha (3:1 H_2SO_4:H_2O_2) at 80^oC for 20 minutes before they were rinsed with water and dried with N_2 gas (information on the surface charge density of quartz can be found in reference 11 and 12); 0.5 nM MTAB-nanorod solution was laid on top of the quartz wafer for 15 minutes; the excessive nanorod solution was removed by dipping the sample in a pool of fresh methanol; the sample was further rinsed with fresh methanol from a glass dropper by five times and finally the sample was dried with N_2 gas. In this way I electrostatically immobilized monolayer MTAB-covered octagonal Au nanorods on the quartz surface.

Procedures for the assembly of CTAB-coated Au nanorods on quartz are similar yet the yield of a good sample is much lower for reasons not quite clear yet. Single crystal quartz wafers were first activated by piranha (3:1 H_2SO_4:H_2O_2) at 80^oC for 20 minutes before they were rinsed with water and dried with N_2 gas; 10 nM MTAB-nanorod solution was laid on top of the quartz wafer for 60 minutes; the excessive nanorod solution was removed by dipping the sample in a pool of fresh ethanol; the sample was further rinsed with fresh ethanol from a glass dropper by five times and finally the sample was dried with N_2 gas. Note the CTAB coating becomes a monolayer because ethanol should have dissolved the outer leaflet of CTAB which is bound to the inner leaflet only by weak van der Waals forces.

The yield of a good sample of CTAB-nanorod on quartz is lower than that of

MTAB-nanorod on quartz. In retrospect, I think this is because most of the CTAB-nanorod solutions I used contain a certain concentration of free CTAB. This concentration may be higher than the threshold concentration at which the screening effect by the CTAB electrolyte starts to slow down the deposition of CTAB-nanorod on quartz. I am not sure if the minimum CTAB concentration I can get by the method of centrifugation is lower or higher than the threshold concentration when screening effect starts to take place; I think it is lower. It is better if one can keep track of the CTAB concentrations during the centrifugation and immobilization processes and eventually figure out what is the minimum CTAB concentration one can reliably get by centrifugation, and what is the threshold CTAB concentration when the screening effect starts to take place.

For the immobilization of MTAB-nanorods on quartz, the dispersant and washing fluid are selected from two solvents: water and methanol, both of which can disperse MTAB-nanorods well. There are four combinations for the dispersant and washing fluid and I chose water as the dispersant and methanol as the washing fluid based on the following considerations. The goal is to create a large-area, spatially-uniform, non-aggregated nanorod-covered surface. The dispersant needs to be a slowly-evaporating solvent, otherwise the nanorod concentration will have spatial variations due to solvent evaporation, and the receding of the droplet will induce aggregation of the nanorods. Dry-out of the solvent will lead to the formation of a nanorod film and apparently such a film will exhibit different transient absorption property. The surface tension of the dispersant is better to be big so that one can add enough nanorod solution to cover

the entire quartz surface and at the same time the solution will not smear the other side of the quartz. In this way, water is a better choice for dispersant than methanol. I chose methanol instead of water as the washing fluid because methanol evaporates faster and methanol has a low surface tension so that it will less likely to pull the surface nanorods into aggregates as the pinning line recedes [6]. MTAB-coated nanorods disperse well in methanol so there is no risk of creating nanorod aggregates during the rinsing step. Nanorod aggregates will cause big trouble in the transient absorption measurement.

Au nanorods of different aspect ratio diffuse to the quartz surface at different rates. This can lead to the effect that at an earlier stage of the immobilization process shorter nanorods occupy the quartz surface first. Thermodynamically the surface should favor longer nanorods so at a later stage of the immobilization process, longer nanorods will replace shorter nanorods. According to figure 3.5, the size distribution of the adsorbed nanorods is indeed immersion-time dependent: longer immersion time (15 minutes) results in a size distribution centered at an aspect ratio of 3.7 (λ_{max}=770 nm) and shorter immersion time (5 minutes) results in a size distribution centered at an aspect ratio of 3.1 (λ_{max}=710 nm). In addition, the higher nanorod concentration correlates with a higher surface coverage. Finally, I found 15 minutes is long enough for the nanorods to reach thermodynamic equilibrium on the quartz surface.

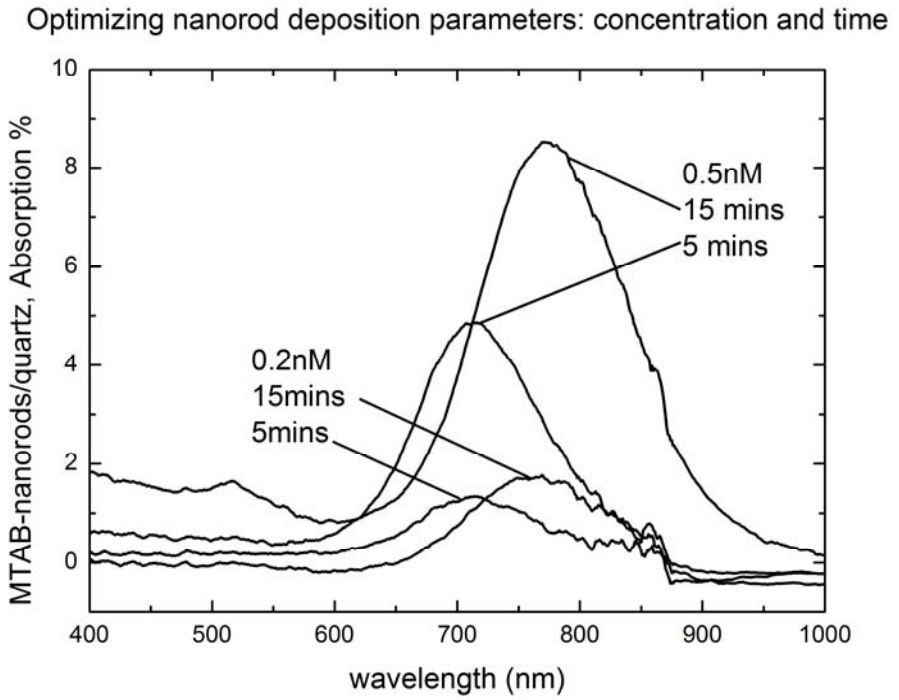

Figure 3.5: UV-vis absorption spectra of four samples of MTAB-nanorods on quartz. I used the same pellet of MTAB-nanorods to make two solutions: one is a 0.2 nM nanorod solution and the other is a 0.5 nM nanorod solution. Their concentrations are measured by independent UV-vis absorbance measurements. Different immersion time (5 mins and 15 mins) was tested using these two nanorod solutions.

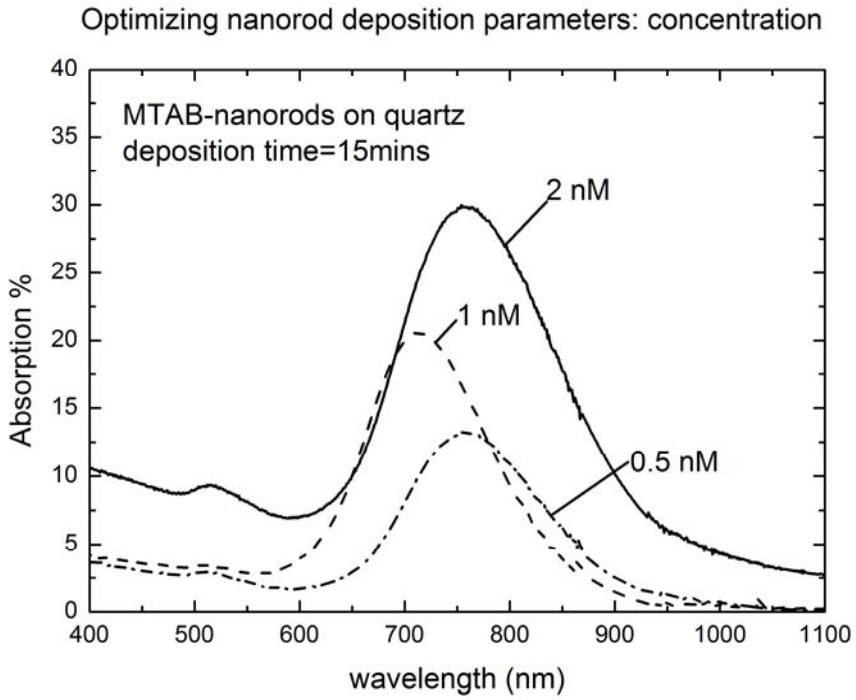

Figure 3.6: Optimizing the concentration of MTAB nanorods. Three concentrations were used and the immersion time was 15 minutes.

Empirically, the optimal surface coverage is attained when the maximum absorption is between 5% to 15%. If the maximum absorption of a sample reaches 30%, the coverage is too high and a lot of nanorods will form aggregates on the quartz surface. The optimal MTAB-nanorod concentration is 0.5 nM (figure 3.6).

3.1.6 Size characterization of CTAB-coated and MTAB-coated Au nanorods

I characterized the size of MTAB-coated and CTAB-coated Au nanorods and their assemblies on quartz by transmission electron microscopy (TEM), UV-vis spectrophotometry and scanning electron microscopy (SEM). The average length and width of MTAB-coated Au

nanorods shown in figure 3.7 were 44.7 nm (std = 5.5 nm) and 12.5 nm (std = 2.0 nm) separately, as determined from the TEM images of 80 MTAB-coated Au nanorods coming from the same sample. The maximum optical absorption and the surface coverage of MTAB-Au nanorods on quartz was 8.5% and 6.5% respectively hence I determined the ratio of the maximum optical absorption to the surface coverage to be 1.3 for MTAB-Au nanorods (figure 3.7). This number is close to 1.2 for CTAB-Au nanorods [13]. The SEM image shows the nanorods are well-separated from each other; the symmetric line shape of the longitudinal surface plasmon resonance (LSPR) and the zero absorption at 1100 nm are also indications that the Au nanorods are non-aggregated.

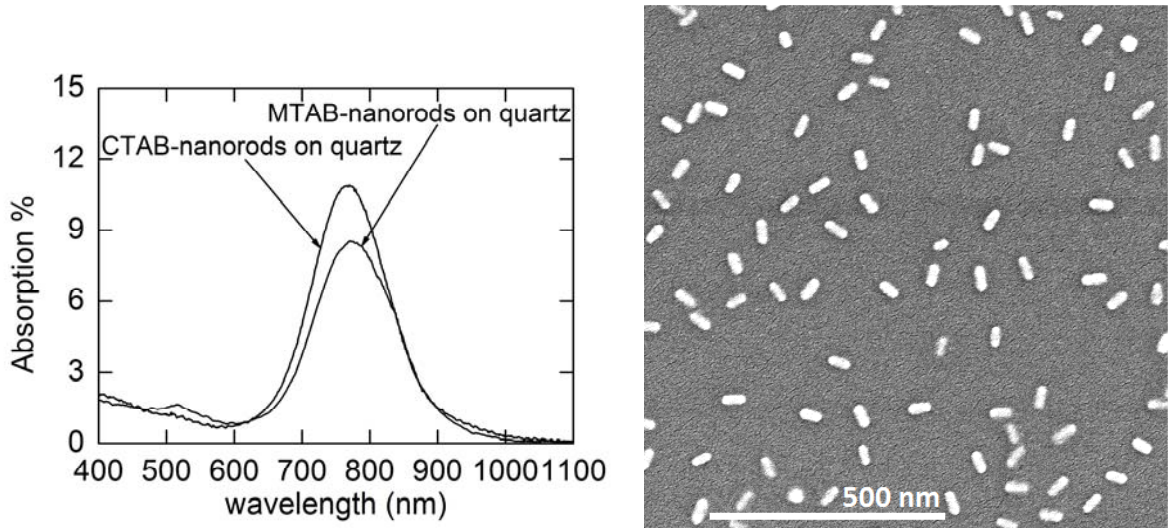

Figure 3.7: (a) Optical absorption spectra for MTAB- and CTAB-coated Au nanorods on quartz. Spectra were obtained from the measurements of optical transmittance and reflectance on a UV-vis spectrophotometer. (b) Scanning electron microscopy (SEM) image of MTAB-coated Au nanorods on quartz. A thin layer of Al was sputtered on the sample to make it electrically conductive before the SEM characterization.

3.1.7 Characterization of the monolayer of MTAB around Au nanorods

I prepared three samples at the same time and simultaneously loaded them into the XPS instrument: the first sample was made by dropping 0.5 mL of 1 nM purified MTAB-nanorod solution on a piranha-activated quartz wafer and letting the sample dry naturally for 1 day. The second sample was made by dropping 0.5 mL of 1 nM twice-centrifuged CTAB-nanorod solution on a quartz wafer and letting the sample dry naturally for 1 day. The CTAB concentration in the nanorod solution was 0.1 mM so a lot of free CTAB was also present around the CTAB-nanorods. The third sample was a piece of piranha-activated quartz wafer serving as a control sample, which was preserved next to the other two samples.

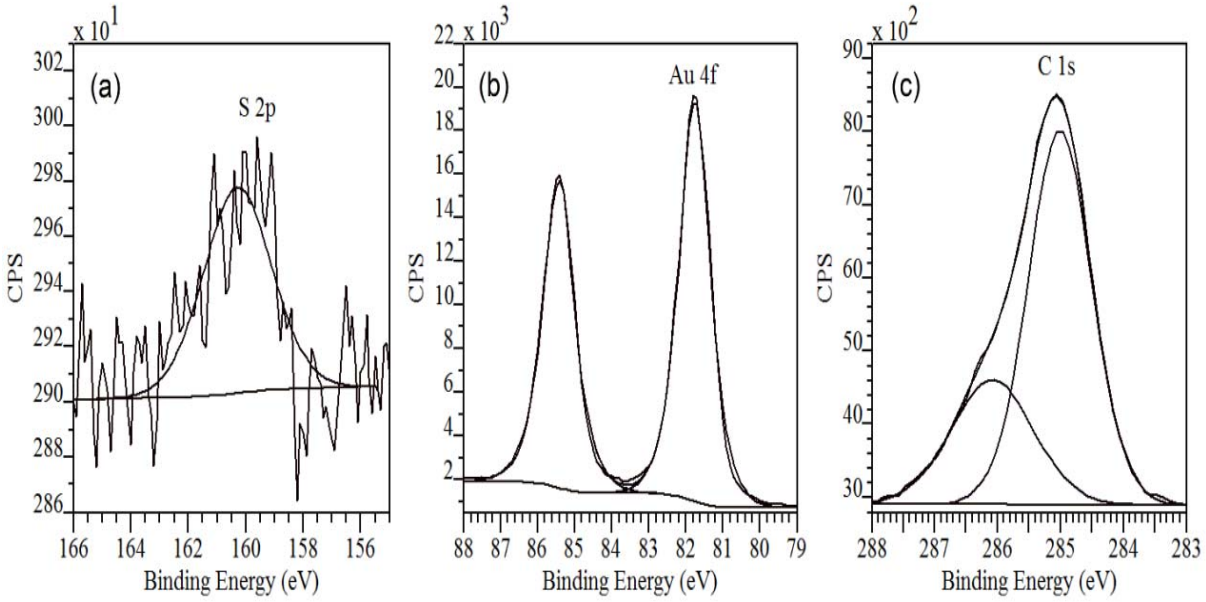

Figure 3.8: High resolution XPS spectra of the S 2p (a), Au 4f (b) and C 1s (c) regions of a film of MTAB-Au nanorods on quartz. The sample was made from evaporation of the purified MTAB-Au nanorod solution. The X-ray source is Al Kα line at 1486.6 eV and the take-off angle

is 90^{o}. The three high resolution spectra were collected each with 1 hour acquisition time. The background subtraction was Shirley type and the peaks were fit with Gaussian/Lorentzian line shape.

Quantitative X-ray photoelectron spectroscopy (XPS) can be used to determine the coverage of S atoms on the surface of Au nanorods. I need this number to calculate the volumetric heat capacity of MTAB. In XPS, the thickness of a top layer or the coverage of the adsorbates can be determined by comparing the photoelectron intensity of an element in the top layer (adsorbates) and that of an element in the bottom layer [14]. The ratio of the S 2p intensity to the Au 4f intensity is a function of the number densities of S/Au atoms, the thickness of each layer, the photoelectron cross sections (i.e., relative sensitivity factor) and the extent of photoelectron attenuation in these layers. Since the kinetic energy of S 2p photoelectrons (1327 eV) is close to the kinetic energy of Au 4f photoelectrons (1403 eV), determination of the number of S atoms per unit area is less sensitive to the thickness and effective attenuation length of photoelectrons of the MTAB layer; instead, it is sensitive to the attenuation length of Au 4f photoelectrons in metal Au, which has been determined accurately. For a submonolayer of S atoms coating a Au cylinder, I want the extent of attenuation to be accurately accounted for, so I make use of previous theoretical work [15] – a layer-on-cylinder model inside the XPS MultiQuant software [16]. Parameters needed in this model such as the effective attenuation lengths of photoelectrons are obtained from the NIST electron EAL database and other references [17,18]. The number of S atoms per unit area was found to be 3.5 ± 0.7 nm^{-2} which is

in good agreement with the packing density of 3.7 nm^{-2} determined from thermogravimetric analysis (TGA) [3]. The packing density of MTAB on Au nanorods is smaller than the packing density of more typical linear alkanethiols on Au(111) texture (4.5 nm^{-2}) [19] possibly because of the steric and electrostatic repulsions between the tertiary ammonium groups.

The number of C atoms per unit area of MTAB-Au nanorods on quartz was much higher than expected (126 nm^{-2}) – corresponding to 36 rather than 19 C atoms per S atom – which I attribute to the "shadow effect" [14] occurring in the superlattice-like structure of close-packed MTAB-Au nanorods: at 90^{o} take-off angle, Au 4f and S 2p photoelectrons from deep inside the film are blocked by the surface Au nanorods, while C 1s photoelectrons can have a larger escape depth. The carbon coverage of a nominally clean quartz substrate was small (8 nm^{-2}) and the free MTAB concentration was estimated to be 1000 times smaller than the concentration of MTAB-Au nanorods therefore the hydrocarbon contamination as well as the free MTAB molecules cannot be the explanations for the apparently large carbon content. I used the electron effective attenuation length of other SAMs [18] which may cause inaccuracy in determining the carbon density.

Other information contained in the XPS spectra (figure 3.8, 3.9 and 3.10) was also consistent with the proposed geometry (figure 3.3). The relatively low binding energy of S 2p photoelectrons (160.3eV) suggests the S atoms are in low oxidation state [20]. I expect the S atoms to bind with the Au nanorod and have a low oxidation state. Note all binding energies are referenced to the C 1s line at 285.0 eV. In addition, two C 1s components show up in the XPS

spectrum. One at 286.1 eV comes from the C atoms binding to N/S atoms and the other at 285.0 eV comes from the C atoms binding only to C atoms. The ratio of the intensities of the two components is 0.4, which is consistent with the numbers of these two groups of C atoms: 5/14=0.36. Moreover, the ratio of N 1s intensity to Br 3d intensity was 94% of the ratio of their relative sensitivity factors (R.S.F.). Since the N atoms are paired with Br atoms, the consistency between the intensity ratio and the R.S.F. ratio indicates that N and Br are indeed 1:1. Finally, the ratio of S 2p intensity to N 1s intensity is consistent with the ratio of R.S.F. times the attenuation by the SAM layer.

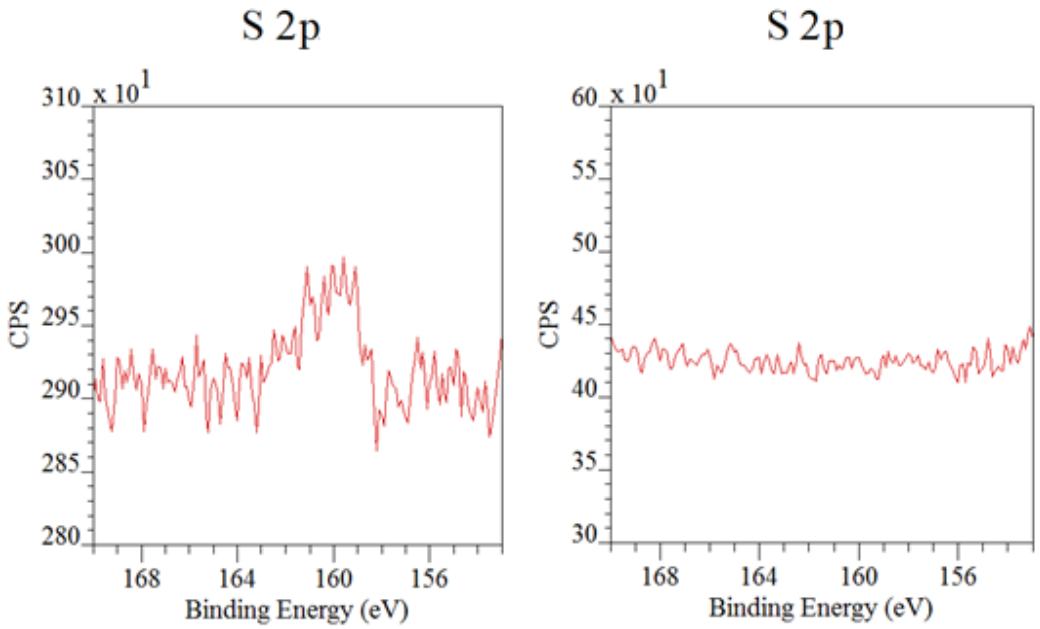

Figure 3.9: The sample of MTAB-nanorods has a S 2p photoelectron peak while the sample of CTAB-nanorods doesn't. The X-ray power, the take-off angle and the acquisition time are the same for the two samples. The background and shot noise in the left spectrum arise from the a lot more inelastically scattered Au 4f photoelectrons from the sample of MTAB-nanorods.

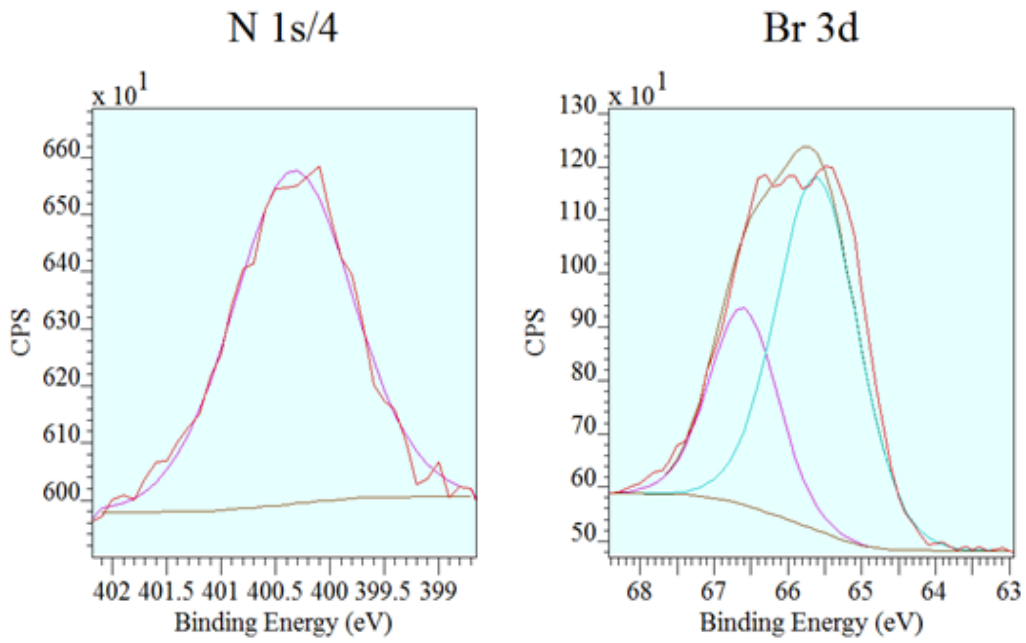

Figure 3.10: High resolution XPS spectra of the N 1s (left) and Br 3d (right) regions of a film of MTAB-Au nanorods on quartz. The colored lines show the Shirley background subtraction and the Gaussian/Lorentzian line fitting.

3.2 Thermal modeling

A typical plot of transient absorption data of MTAB-coated nanorods on quartz is given by figure 3.11. The in-phase signal will always be converted to the change in optical transmittance first using the equation 2.1. The data is comprised of four features [7], namely the initial spike due to nonequilibrium hot electrons, the acoustic oscillations due to the coherent excitation of nanorod vibrations, a single exponential component – which is a straight line in the log-linear plot – with a characteristic time of a few hundreds of picoseconds, and a fast decay component with a characteristic time of a few tens of picoseconds. The fast decay component at short time

scale and the single exponential component at long time scale separately represent the heat transfer from the Au nanorods to the coating molecules and the heat transfer from the coating molecules to the quartz substrate.

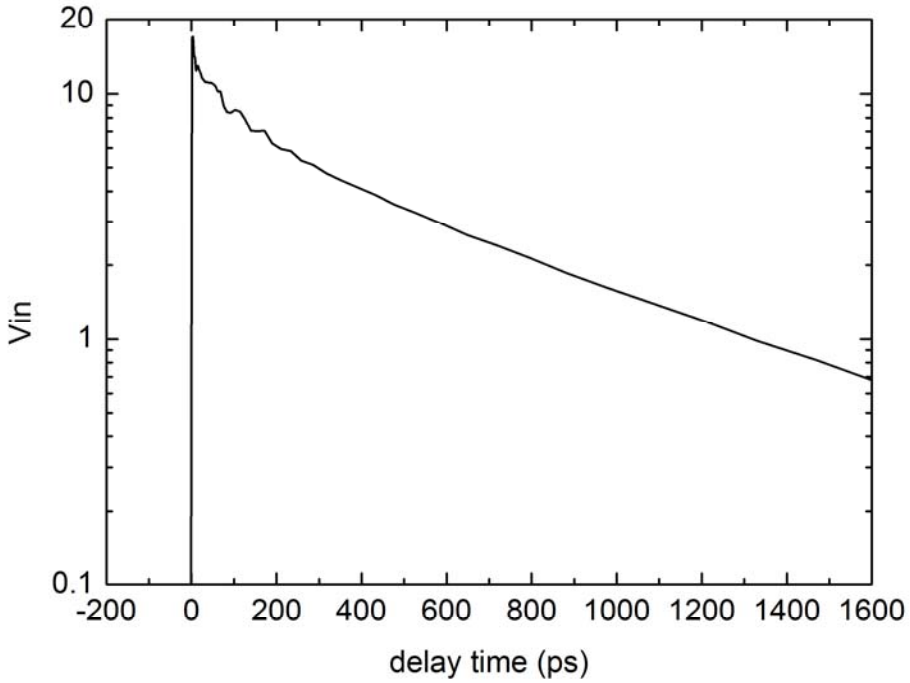

Figure 3.11: transient absorption data of MTAB-coated nanorods on quartz. Vin is the in-phase signal from the lock-in amplifier. (See section 2.1.2)

I analyze the experimental data with a bidirectional heat transfer model. I assumed the side facets of the octagonal Au nano-cylinders were lying flat on the surface, which created a planar interface. The opposite charges on the nanorods and the quartz should have brought them into close contact. Nanorods standing on their end facets were not aligned with the in-plane electric field of the laser therefore they contribute little to the transient absorption signal. Next, the

geometry of “octagonal Au nano-cylinders lying flat on quartz surface” was approximated to a layered structure (figure 3.12). From top to bottom the layers are MTAB (or CTAB, which has the same thickness with the MTAB coating), MTAB/Au interface, Au (which has the same cross section with the Au nanorod), Au/quartz interface and quartz. Heat was deposited in the Au layer and began to diffuse along both directions, hence the model is named “bidirectional heat transfer model”. The top layer of the model represents the molecules coating seven side-facets of the Au nanorod therefore the volumetric heat capacity and the thermal conductivity of this molecular layer are multiplied by 7 times. A layer of Au can represent the Au cylinder because Au has negligible thermal resistance. The Au/quartz interface has some finite heat capacity because it represents the molecules sandwiched between the Au and the quartz. The volumetric heat capacity and thermal conductivity of quartz were assumed to be infinity. This is because when I numerically solved the heat equation using the PDE tool from Matlab, I found the temperature of quartz next to the interface remained 20 times smaller than the temperature of Au at all times.

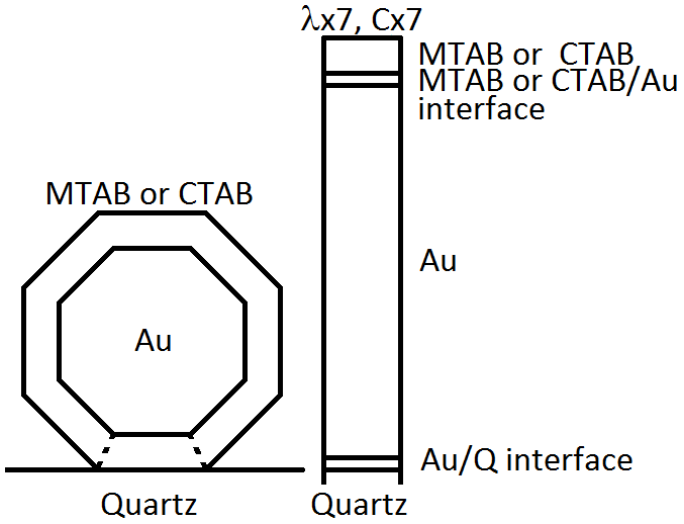

Figure 3.12: Schematic diagram of the real geometry (left) of Au nanorods on quartz and the

(Figure 3.12 cont.) corresponding geometry (right) that I used to model the experimental data. The two boundaries and the molecules enclosed by them (between the dashed lines) are treated as a single Au/quartz interface. The typical width of a side-facet of the Au nanorod is 5 nm and the typical thickness of the molecular layer is 2.5 nm.

The temperature of Au in the bidirectional model was calculated using an analytical solution to the heat diffusion equation in cylindrical coordinates [21], which was then multiplied with a free-adjusting parameter so that the modeled data fit the experimental data at 20 ps. This delay time was chosen by the time at which the hot electrons have equilibrated with the Au lattice and no much heat had leaked into the coating molecules or the substrate.

I adjust two free parameters, the thermal conductance of MTAB/Au and the thermal conductance of Au/quartz to model the experimental data. The parameters, i.e., thickness, heat capacity and thermal conductivity, of each layer are obtained following the approximation introduced above as well as the considerations given below. The heat capacity and thermal conductivity of Au are fixed by literature values [22]. At all temperatures I used 5 W m^{-1} K^{-1} for the thermal conductivity along the bounded MTAB or CTAB molecules. This is because the thermal conductance of the MTAB/Au interface was small which dominated the heat conduction into the molecular layer. It takes a little more effort to figure out the volumetric heat capacity of MTAB: the volumetric heat capacity of MTAB is the product of the heat capacity of branched polyethylene per mole of (CH_2) [23] and the number of CH_2 segments per unit volume of MTAB. Here I assume there are 21 CH_2 segments per MTAB molecule. To determine the number of CH_2

segments per unit volume of MTAB, I first estimate the thickness of MTAB: MTAB on Au must have attained maximum coverage (3.5 nm^{-2}) so I assume all molecular axes in MTAB are perpendicular to the Au plane. This structure of MTAB is similar to the structure of single crystal polyethylene (PE), although the chain density of MTAB is lower than that of single crystal PE (5.4 nm^{-2}). The thickness of MTAB is therefore 10 * 0.2547 = 2.55 nm, where 0.2547 nm is the height of a unit cell of PE containing (CH_2CH_2) [24]. In this way I obtained the thickness of MTAB, the number of CH_2 segments per unit volume of MTAB and eventually the volumetric heat capacity of MTAB. I cannot measure the packing density of CTAB on Au using XPS because I cannot remove the free CTAB molecules from the nanorod solution. However, I found that using 60% of the packing density of MTAB for the packing density of CTAB, I can obtain a good fit to the CTAB data at all temperatures. An example fit of the transient absorption data for MTAB-Au nanorods is given by figure 3.13.

There has been some ambiguity about the shape of the Au nanorods. A few works believe the cross section of Au nanorods is pentagonal [7,13] so I analyzed the heat transfer assuming pentagonal shape as well. The thermal conductance is displayed in figure 3.14 (b).

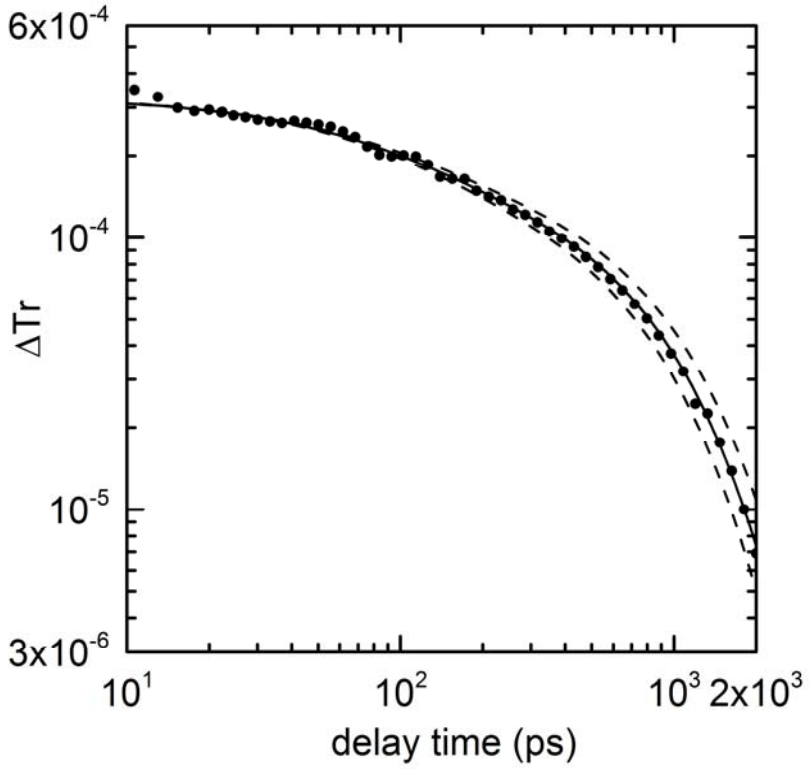

Figure 3.13: Changes in optical transmittance ΔTr for the MTAB-Au nanorods on quartz plotted as a function of delay time between the pump and probe laser pulses. The fitting data are multiplied with a free-adjusting parameter so that they fit the experimental data at 20 ps. The solid line is the best fit to the experimental data using G(Au/Q)=155 MW m^{-2} K^{-1} as the thermal conductance of the Au/quartz interface. The dash lines are calculations using G(Au/Q)=170 MW m^{-2} K^{-1} and G(Au/Q)=140 MW m^{-2} K^{-1} demonstrating the sensitivity of the measurements.

3.2.1 Per pulse heating

In the above thermal modeling, I have assumed the heat capacity of each layer stays

constant across the whole range of delay time. This is true in the regime of small temperature excursions. The threshold that I use is the per pulse heating of the mostly heated nanorod shall not exceed 30% of the temperature of the sample. In the low temperature measurements, I used a pump beam of 1.5 mW above 150 K; below 150 K, I used a pump power that is a linear function of temperature: 0.3 mW at 50 K increasing to 1.5 mW at 150 K. The power of the probe beam was the same with the power of the pump beam. The maximum temperature excursion (per pulse heating) of the most heated Au nanorods is calculated by dividing the per pulse energy absorbed by the nanorods with the heat capacity of the nanorods: for example, at 150 K, using 1.5 mW as the pump power, 1.2 as the ratio of optical absorption to surface coverage and 12.5 nm as the diameter of the Au nanorods, the per pulse heating averaged over all Au nanorods within the circle of rms radius is 4.7 K. The per pulse heating was not uniform for these nanorods [13]. The inhomogeneously broadened LSPR peak of the sample is 4 times wider than the homogeneous peak width, so the peak temperature excursion will be about 4 times larger than the average. In addition, the laser power at the center of the Gaussian beam is twice as large as the average laser power so the most heated Au nanorods had a per pulse heating of 4.7 K * 2 * 4 ≈ 38 K, which is 25% of 150 K.

3.3 Results and discussions

The thermal conductance of the Au/quartz interface can be written as follows [25]:

$$G(T) = \frac{1}{V}\frac{\partial}{\partial T}\sum_{kj}^{Au} \hbar\omega_{kj} n(\omega_{kj}, T)\left|v_{kjz}\right| t_{kj} = \frac{1}{V}\frac{\partial}{\partial T}\sum_{kj}^{quartz} \hbar\omega_{kj} n(\omega_{kj}, T)\left|v_{kjz}\right| t_{kj} \quad , \tag{3.1}$$

where the ω is the phonon frequency, n is the Bose-Einstein distribution function, v is the component of the phonon group velocity normal to the interface, t is the transmission probability and the sums are over all phonons in the Brillouin zone. I choose to evaluate the transmission probability t(ω) from the quartz side because the Debye temperature of quartz (470 K) is greater than the Debye temperature of Au (165 K) [26]: at a frequency $\omega \le \omega_{\max}(Au)$ the phonon flux is always greater from the Au side; at a frequency $\omega > \omega_{\max}(Au)$ no phonons can transport across the interface, if I assume all scattering at the interface is elastic, hence the maximum possible conductance is attained when t(ω)≡1 evaluated from the quartz side (phonon radiation limit) [25]. Because only long-wavelength acoustic phonons involve in the transport, quartz can be approximated as elastic continuum. If elastic isotropy as well as incident-angle independence of transmission probability are further assumed, the angular integral reduces to $\frac{1}{4}$ and the following equation is obtained:

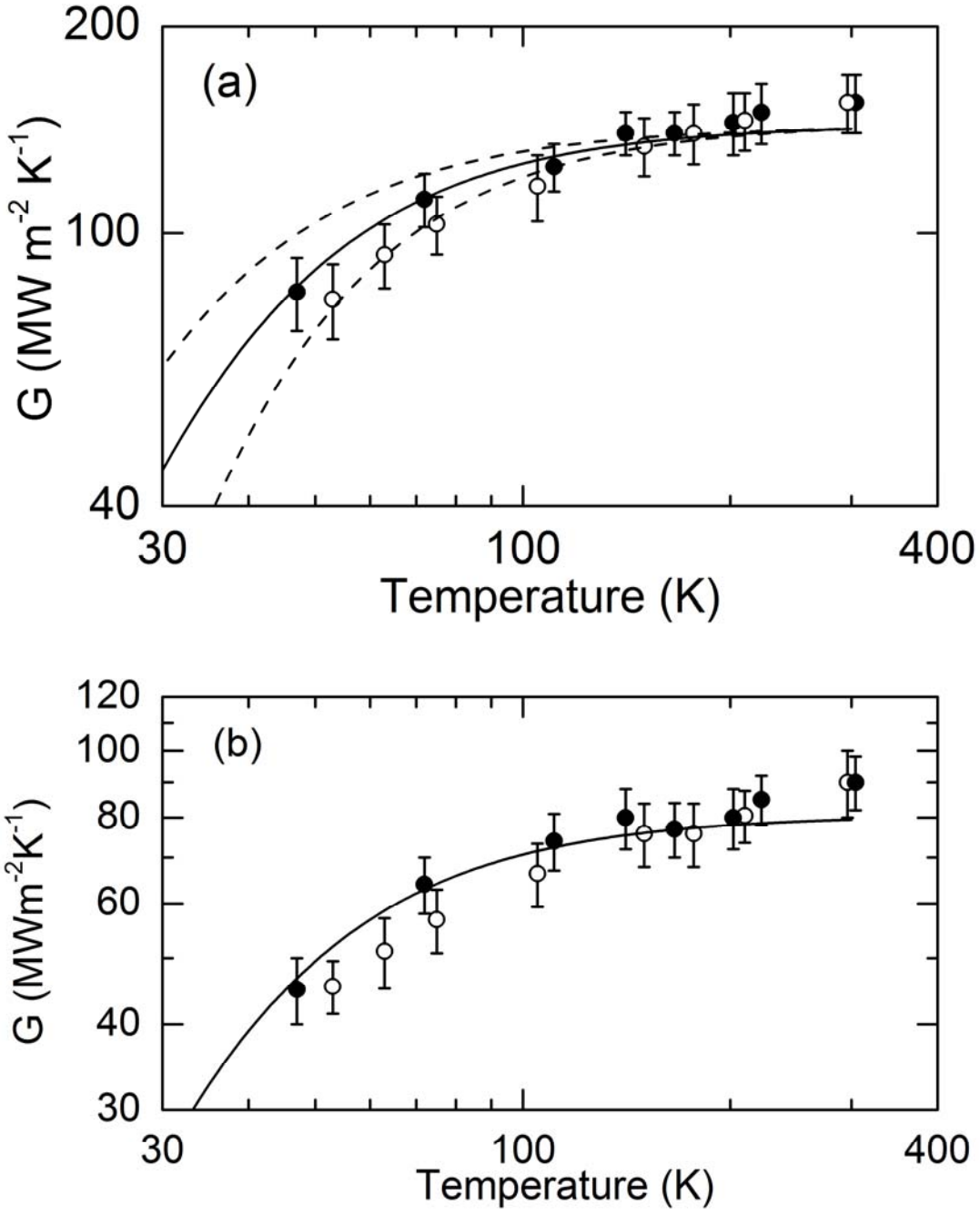

Figure 3.14: (a) Thermal conductance G of the Au/quartz interface for the MTAB-Au nanorods on quartz (solid circles) and the CTAB-Au nanorods on quartz (open circles) plotted as a function of temperature. The solid line is scaled by the temperature dependence of the Debye

(Figure 3.14 cont.) heat capacity (Θ=165 K). The lower dashed line is scaled by the temperature dependence of the integral in equation (3) using $t(\omega)=1, \omega \in [0.8\omega_{\max}, \omega_{\max}], otherwise, t(\omega)=0$ and the upper dashed line is scaled by the temperature dependence of the integral in equation (3) using $t(\omega)=1, \omega \in [0, 0.8\omega_{\max}], otherwise, t(\omega)=0$. All three theoretical curves are normalized at 142 MW m^{-2} K^{-1} at 300 K. (b) thermal conductance analyzed by assuming pentagonal shape of the Au nanorods.

$$G(T)=\frac{1}{8\pi^2}\left[\frac{1}{c_l^2}+\frac{2}{c_t^2}\right]\int_0^{\omega_{\max}}\frac{\partial n(\omega,T)}{\partial T}t(\omega)\hbar\omega^3 d\omega, \tag{3.2}$$

where the c_l and c_t are the longitudinal and transverse sound velocities of quartz and ω_{max} is the Debye frequency of Au. The Debye frequency of Au is 3.3 THz while the maximum frequency of the true vibrational spectrum of Au is 4.5 THz [28]. The Debye heat capacity per unit volume at a frequency ω is given as follows:

$$C(\omega,T)d\omega=\frac{\partial n(\omega,T)}{\partial T}\hbar\omega\frac{3\omega^2}{2\pi^2 c_{Au}^3}d\omega, \tag{3.3}$$

where the c_{Au} is the Debye speed of sound for Au. I replace the ∂n/∂T term with the Debye heat capacity of Au at frequency ω:

$$G(T)=\frac{1}{4}\frac{c_{Au}^3}{c_q^2}\int_0^{\omega_{\max}}t(\omega)C_{Au}(\omega,T)d\omega, \tag{3.4}$$

where the c_q is the Debye speed of sound for quartz. In equation (5) it is clearly seen that if t(ω)

is a uniform function of ω, G(T) is related to the Debye heat capacity of Au with a constant and their temperature dependence should scale the same. Our measurements show that the temperature dependence of G(Au/quartz) for both MTAB- and CTAB-Au nanorods on quartz indeed scales in the same way with the temperature dependence of the Debye heat capacity of Au (figure 3.15 solid line).

To get a better insight for the functional form of t(ω), I evaluated the integral in equation (3) using three different functional forms of t(ω):

$$\begin{aligned} &t(\omega) \equiv 1; \\ &t(\omega) = 1, \omega \in [0.8\omega_{\max}, \omega_{\max}], otherwise, t(\omega) = 0;, \\ &t(\omega) = 1, \omega \in [0, 0.8\omega_{\max}], otherwise, t(\omega) = 0. \end{aligned} \tag{3.5}$$

The temperature dependence of the evaluated integral is displayed in figure 3.15.

Organic materials have been speculated to facilitate inelastic scattering because of their bonding anharmonicity [27]. Our measurements of G for both MTAB- and CTAB-Au nanorods at 300 K are only 10% (within experimental error) more than the G measured at the Debye temperature of Au. The plateau of G above the Debye temperature of Au suggests inelastic scattering isn't a significant contributor to the interfacial thermal transport.

In summary, I have measured the interfacial thermal conductance *G* of a self-assembled monolayer of molecules (MTAB and CTAB) between Au and quartz as a function of temperature in the range 40 < T < 300 K. The temperature dependence of the thermal conductance has the same form as the temperature dependence of the Debye heat capacity of Au. This result suggests the spectrum of vibrational modes that carry heat through the interfaces is similar to the

vibrational spectrum of Au. Assuming Au and quartz are both Debye solids, I have further analyzed the interfacial thermal conductance using three functional forms of the transmission probabilities t(ω) from the quartz side. I conclude that the phonon transmission probability across such a molecular interface is biased neither towards high frequency phonons nor towards low frequency phonons and that inelastic scattering isn't significantly contributing to the heat transport in such systems.

3.4 References

[1] T. K. Sau and C. J. Murphy, Langmuir **20**, 6414 (2004).

[2] S. Link, M. Mohamed, and M. El-Sayed, J. Phys. Chem. B **103**, 3073 (1999).

[3] L. Vigderman, P. Manna, and E. R. Zubarev Angew. Chem. Int. Ed. **51**, 636, (2012).

[4] N. Balachander and C. N. Sukenik, Langmuir **6**, 1621 (1990).

[5] C. J. Murphy, L. B. Thompson, A. M. Alkilany, P. N. Sisco, S. P. Boulos, S. T. Sivapalan, J. A. Yang, D. J. Chernak, and J. Huang, J. Phys. Chem. Lett. **1**, 2867 (2010).

[6] B. P. Khanal and E. R. Zubarev, Angew. Chem. Int. Ed. **46**, 2195 (2007).

[7] G. V. Hartland, Phys. Chem. Chem. Phys. **6**, 5263 (2004).

[8] Nikoobakht, B.; El-Sayed, M. A. Chemistry of Materials **10**, 1957, (2003).

[9] Goris, B., Bals, S., Van den Broek, W., Carbó-Argibay, E., Gómez-Graña S., Liz-Marzán, L. M., Van Tendeloo G. Nature materials **11**, 930, (2012).

[10] Nikoobakht, B., El-Sayed, M. A, Langmuir **20**, 6368, (2001).

[11] Leung, K., Nielsen, I. M., Criscenti, L. J, J. Am. Chem. Soc. **51**, 18358, (2009).

[12] Ong, S., Zhao, X., Eisenthal, K. B. Chem. Phys. Lett. **3**, 327, (1992).

[13] J. Park, J. Huang, W. Wang, C. J. Murphy, and D. G. Cahill, J. Phys. Chem. C **116**, 26335 (2012).

[14] Oura, K., Saranin, A. A., Zotof, A. V. *Surface science: an introduction;* Springer Berlin: (2003).

[15] Mohai, M., Bertoti, I. Surf. Interface Anal. **8**, 805, (2004).

[16] Mohai, M. Surf. Interface Anal. **4**, 640, (2006).

[17] Powell, C., Jablonski, A. J. Surf. Anal. **3**, 322, (2002).

[18] Bain, C. D., Whitesides, G. M. J. Phys. Chem. **4**, 1670, (1989).

[19] Love, J. C., Estroff, L. A., Kriebel, J. K., Nuzzo, R. G., Whitesides, G. M. Chem. Rev. **4**, 1103, (2005).

[20] Moulder, J. F.; Chastain, J.; King, R. C. *Handbook of X-ray photoelectron spectroscopy: a reference book of standard spectra for identification and interpretation of XPS data;* Physical Electronics Eden Prairie, MN: 1995

[21] Cahill, D. G. Rev. Sci. Instrum. **12**, 5119, (2004).

[22] Touloukian, Y. *Thermophysical Properties of Matter*, New York (1970)

[23] Chang, S.; Westrum, E.; Carlson, H. G. Journal of research of the National Bureau of Standards.Section A.Physics and chemistry **2**, 437, (1975).

[24] Yin, L.; Chen, J.; Yang, X.; Zhou, E. Polymer **21**, 6489, (2003).

[25] Stoner, R.; Maris, H. Phys. Rev. B **22**, 16373, (1993).

[26] Kittel, C., McEuen, P. *Introduction to solid state physics;* Wiley New York: 1996; Vol. 7

[27] Losego, M. D.; Cahill, D. G. Nature materials **12**, 382, (2013).

[28] W. L. Ong, S. M. Rupich, D. V. Talapin, A. J. H. McGaughey, and J. A. Malen, Nature Materials **12**, 410, (2013)